Mechanisms-Based Fracture Model for Geological Materials

Tobias Hoeink

Baker Hughes

Alek Zubelewicz

Alek & Research Associates

Abstract: Over the past decade, hydraulic fracturing has become an industry-changing technology that enables commercial production of hydrocarbons from previously non-productive low-permeability shale formations. R&D efforts focus on the development of economically efficient production protocols, where the selection of engineering solutions is guided by numerical simulations. Typically, the simulations are based on phenomenological fracture models that are adapted for the prediction of fluid-driven fracture processes at depth. These models rely on a long-term trial-and-error approach and offer reliable material response at conditions that have previously been experimentally investigated. For this reason, an extrapolation of such phenomenological models into untested regimes is not always successful.

We break with the tradition of using phenomenology and, instead, construct a mechanisms-based fracture model for geological materials. Our modified Mohr-Coulomb fracture model is developed in the framework of tensor representation theory, which allows for a direct translation of fracture mechanisms and the observed inelastic deformation into a mathematically precise description. In our description, plastic deformation is rate dependent and dilatation is determined over a three-dimensional topography of the slip plane. The contribution of asperity degradation is also included. The model monitors crack orientations and, in this manner, adds to the fracture-induced anisotropy. Fracture strength is stochastic. We also introduce an effective stress that accounts for the hydraulic pressure deposited onto crack surfaces. Friction-induced damage and tensile fractures are the sources of an enhanced hydraulic permeability. Our permeability model is also stochastic, and it describes the formation of flow-channels due to the coalescence of micro-cracks in tension and shear. To illustrate the approach we choose material properties applicable to shale. We test the material model using uniaxial tension, compression and triaxial stress conditions on a single element before advancing to relevant subsurface model geometries.

Our current study focuses on the simulation of fluid-driven fracture near a pressurized wellbore. The results demonstrate that fracture growth is often dynamic; inertial forces play a significant role. Because fracture strength is stochastic, the process often becomes dynamically unstable and produces bursts of kinetic energy that propagate away from localized regions of low fracture strength. As expected, friction-induced damages are responsible for the formation of micro-channels, which in turn are connected to the channels formed by the dominant tensile cracks. The model is implemented to Abaqus/Explicit as a material user subroutine. We calibrate the properties of a shale-like material and study the material responses under axial loading and selected subsurface conditions.

Keywords*: Hydraulic Fracturing, Failure, Fracture, Geomechanics, Material Model, Mechanisms, Wellbore.*

1. Introduction

Geological materials in the subsurface are ill-suited to fracture experimentation and modeling. First, the exact physical properties and conditions of subsurface material can never be known precisely. Secondly, a sample extracted from the subsurface experiences a change in stresses and is prone to micro-damages. This limits validity of the test results obtained in laboratory testing. These limitations are carried over to the theoretical modeling of material behavior. A promising approach to model fracture and damage in geological materials under subsurface conditions is a mechanism-based approach. The fundamental assumption is that the selected deformation mechanisms remain relevant across a large range of conditions. In this paper we present a mechanisms-based fracture model for geological materials. The "machinery" of the model is based on the earlier developments in Zubelewicz, et al. (2013) and Zubelewicz, et al. (2014). Also, the model includes results summarized in Zubelewicz (1990) and Zubelewicz (1993). The latter allows for the construction of the Mohr-Coulomb mechanism of plastic flow. The fracture model is implemented in Abaqus as a material model, thus it leverages an existing finite-element analysis solver. We carefully test the material response for a single element under various loading conditions. The model is validated for core samples under axial loading. Subsequently, the model is applied to hydraulically-driven near-wellbore fractures under subsurface conditions.

2. Theoretical Foundation

2.1 Micro-cracks

Micro-cracks occur when a material is subjected to sufficiently severe loading. At the scale of a continuum, small cracks are typically not traced and often are ignored. However, in a collective sense, micro-cracks contribute to the overall damage incurred by the material. Our model considers micro-cracks in both tensile and shear mode. The accumulation of directional micro-cracks leads to fractures. Fractures are path-dependent, i.e., the history of stress conditions is a relevant factor. In our approach, fracture orientations are not co-rotational with stress, Figure 1. We preserve the loading history by adding micro-cracks formed at each step of loading process. In compression and shear, geological materials experience localized damage. Our model captures damage mechanisms in tension and compression. Furthermore, the model predicts the permeability of relevant damage networks.

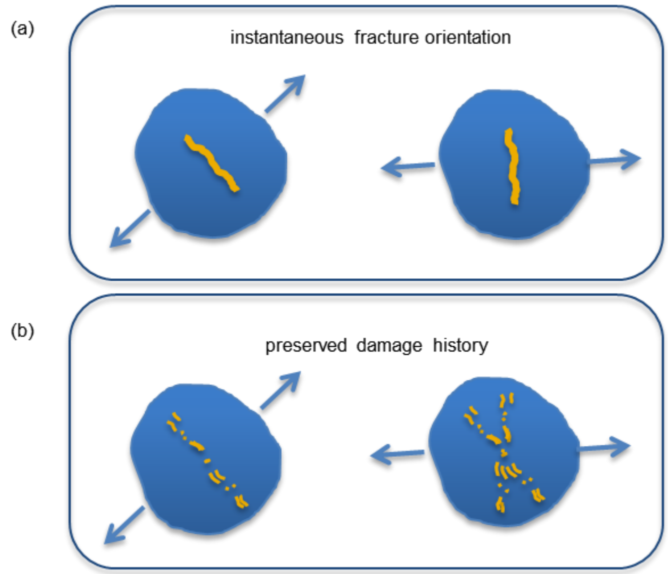

Figure 1. Sketches of different micro-crack modeling approaches. (a) Damage orientation is instantaneously correlated with applied loads. (b) Damage orientations are accumulated during loading history.

2.2 Tensor Representation Theory

Our model is developed in the framework of tensor representation theory (Zubelewicz, 1993). In this framework, relevant physical quantities are expressed in terms of a dyadic product $N_{ij} = n_i n_j$, where n_k is a unit vector. Tensor representation theory states that any symmetric second-order tensor can be represented by another symmetric second-order tensor if both tensors have the same first, second and third invariants. In this formulation, three dyadic products N_{ij} define principal stress orientations. Scalar products of the principal orientation and stresses give the appropriate principal value.

2.3 Modified Mohr-Coulomb Plasticity

In geological materials, plastic deformation is defined in terms of slip and dilatation along rough (non-planar) crack surfaces. When a heterogeneous material is subjected to shear, a slip plane of a rough topography develops. The deformation consists of slip and dilatation (change of volume), where the latter results from the slip plane roughness. In the conventional Mohr-Coulomb model, dilatation results from slip on the plane defined in terms of the minimum and maximum principal stresses. In the modified Mohr-Coulomb fracture model, slip still occurs along the plane defined by the minimum and maximum principal stresses, but dilatation is constructed on three mutually inter-connected planes. Our model is placed in the framework developed for cemented aggregates and geological materials (Zubelewicz, et al., 2013 and Zubelewicz, et al., 2014). Also, we utilize the description of Mohr-Coulomb plastic flow derived in Zubelewicz (1993). The flow tensor is used for the construction of the equivalent stress. Following existing experimental data (Ghanizadeh, et al., 2013), we use an internal friction parameter defined in terms of shale grade, which specifies the kerogen/gas content in liters per ton of shale. The friction parameter is also affected by hydrostatic pressure. Features such as friction, strength and dilatation are sensitive to the material's grade.

Components of the plastic strain rate are defined in terms of the flow tensor, where the magnitude of the flow is defined in terms of the equivalent plastic strain rate. We follow previous descriptions and construct a viscoplasticity constitutive equation, which couples the rate of the equivalent strain with the equivalent stress (Zubelewicz, et al., 2013). In this paper, we use the engineering convention in which compressive stresses and strains have negative values, whereas tensile stresses and strains have positive values. In Figure 2, we compare the stress envelope of the modified Mohr-Coulomb model with the stress envelope of the conventional Mohr-Coulomb model. In the plot, the equivalent stress is scaled by material strength and is presented on the plane of the maximum and minimum principal stresses. Our model is compared with the conventional Mohr-Coulomb description. The difference in shapes of the stress envelopes result from the modified description of plastic dilatation, where the change of volume is affected by the three-dimensional topography of the plane roughness. At advanced shear deformation, the initially rough crack surfaces are grinded. With smoother crack surfaces, the material cannot maintain crack openings and dilatation decreases. The asperity degradation mechanism is developed on the basis of the concept presented in Zubelewicz et al., 1987 and Dowding et al., 1991.

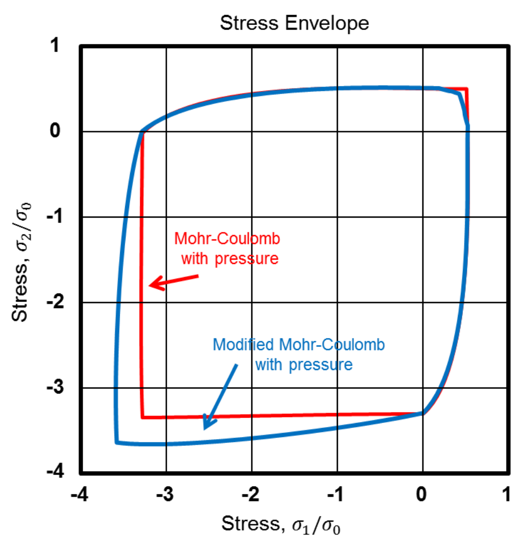

Figure 2. Stress envelopes in the principal stress plane for the modified Mohr-Coulomb model and conventional Mohr-Coulomb model. Equivalent stress is scaled with material strength and pressure dependence is included for both models.

2.4 Damage and Permeability

In shale and other geological materials, permeability results from the interconnection between pore spaces. It is affected by damage induced by geologic and hydraulic stresses. The heterogeneous nature of geologic materials allows cracks to nucleate at distinct locations and grow independently. When stress concentrations from individual cracks overlap, cracks coalesce and create macro-damages. Nucleation and coalescence processes are highly stochastic and depend on the distribution of material properties and stress induced fractures. In compression and shear, the magnitude of plastic deformation results from the damage triggered by micro-crack interactions. We assume that frictional plastic deformation is responsible for the micro-crack inter-connectivity. Friction-induced dilatation and tensile crack openings promote the formation of interlinked branches. These branches become micro-channels suitable for transporting fluids, both injected fluids and fluids trapped in rock formations. At advanced stages of damage, the rate of crack branching decreases. The transition from one state of damage to another can be violent, and may cause dynamic stress reorganization, observable as a dynamic instability.

In the present formulation, the effective permeability has two contributions; they are the reference permeability and the enhanced permeability caused by tensile cracking and damage coalescence in compression. We assume that the fracture coalescence process is stochastic and obeys a Gaussian distribution. Since the dilatation is based on interacting damage planes, its description properly captures the probability of micro-crack coalescence, which in turn is intrinsically linked to an enhanced permeability.

2.5 Fluid-Solid Interactions

We used the effective stress concept developed in Zubelewicz, et al. (2014). In this formulation, hydraulic pressure is imposed directly on crack surfaces. For hydraulic fracture applications, we couple the fluid pressure acting on crack surfaces with the magnitude of the fluid pressure in the wellbore. In our first implementation, we describe the pressure losses due to friction by scaling down the pressure as a function of the distance from the wellbore. In future implementations we plan to fully couple fluid flow processes with material fracture processes.

3. Results

3.1 Material Response

A quality of any material model can be measured in terms of its predictive capability for simple and complex loading conditions. Also, such models must produce robust results in large scale numerical analyses. Often, single element numerical analysis can become an extremely challenging boundary value problem. Indeed, in Mohr-Coulomb descriptions, uniaxial stress and strain loading places the solution into stress envelop corners. For this reason, only when a single-element model is successful in predicting the expected stresses and strains, then one has the confidence that this numerical implementation can be trusted for multi-element assemblies. Thus, we first demonstrate the material behavior using a single element.

The material response for a single, Cartesian 3D element subjected to uniaxial compression and to uniaxial tension is shown in Figure 3. The responses are plotted for axial stresses and strains under unconfined and confined conditions. The uniaxial compression case is shown in Figure 3a, where

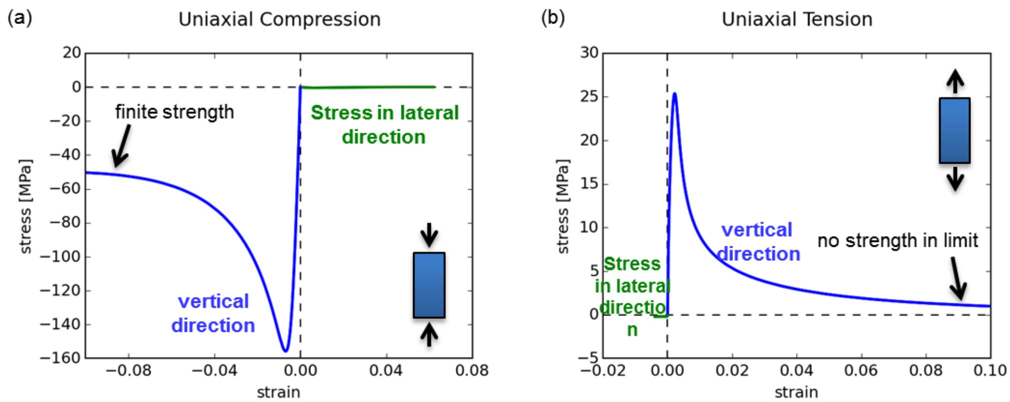

Figure 3. Single element material response in (a) uniaxial compression and (b) uniaxial tension.

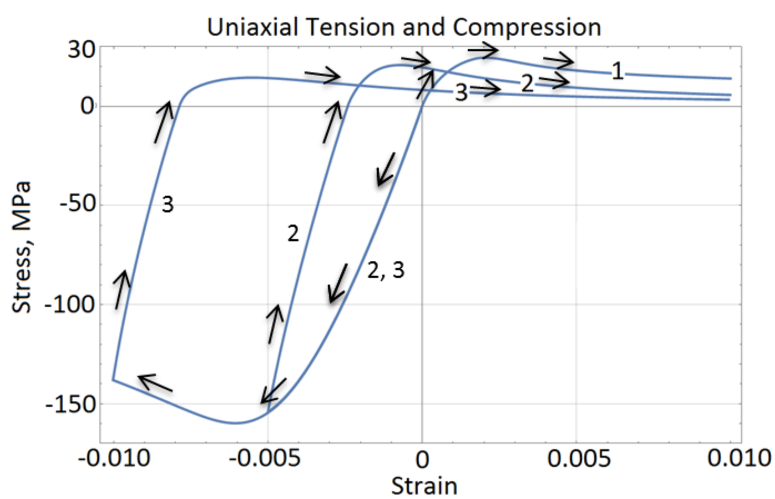

Figure 4. Material responses in uniaxial tension and compression for three different loading curves, each starting at (0,0). Run 1 is a purely tensile loading case, where the material response remains in the upper right quadrant. In contrast, for runs 2 and 3 the material experiences compressive loading first, and the material response curve begins in the lower left quadrant. Initially, runs 2 and 3 follow the same compressive loading path.

the peak stress is in the range of -150 MPa. The post-peak behavior causes elastic degradation, which is responsible for the strain softening behavior. The uniaxial tension test is shown in Figure 3b. The ultimate tensile stress (UTS) is about 25 MPa. Further deformation leads to a rapid elastic degradation and the stress reduction towards zero.

Cycles of uniaxial compressive and tensile loading are plotted in Figure 4. In the first scenario, we apply tensile loading. As in the previous case, UTS is in the range of 25 MPa. In the second run, compressive deformation up to -0.5% strain is applied first and, then, is followed by tensile loading. Compression induced damages reduce tensile strength to 21 MPa. In the third case, compressive deformation is applied to -1% strain and, then, the process is reversed bringing the material to tension. Tensile strength is further reduced; it is 15 MPa.

We further test the model in compression for several strain rates, shown in Figure 5a. We note that the ultimate compressive stress increases at higher strain rates. Also, we test the predictability of the model under triaxial stress conditions, shown in Figure 5b. As observed in tests with real core samples, increasing confining pressure increases material strength.

Additionally, the model captures the effects associated with asperity degradation. As shown in Figure 6a, initially dilatational deformation increases. Further deformation degrades internal friction, thus reverses previous crack opening and decreases dilation. Lastly, we test the responses from subjecting the material to complex loading conditions, where we superimpose the uniaxial strain controlled loading in compression with oscillating lateral stresses, Figure 6b. The combined material responses are shown in Figure 6c. The primary features of the material response of the previous case are reproduced, however the stress cycles significantly reduces the axial peak stress.

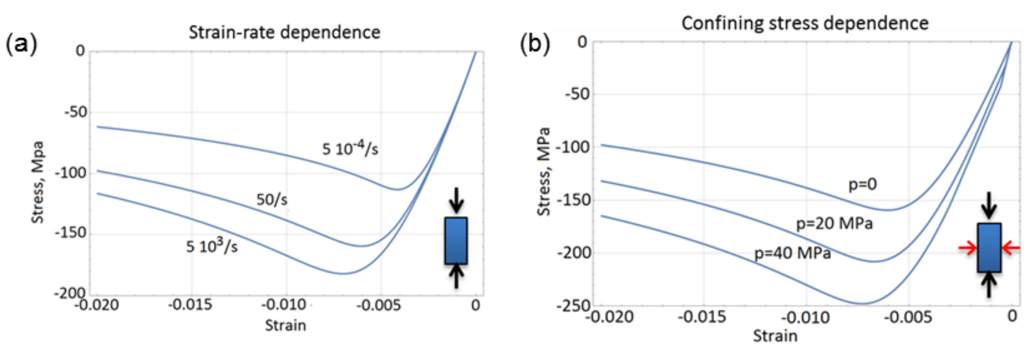

Figure 5. Single element material responses for (a) various strain rates in uniaxial compression and for (b) various confining stresses in triaxial compression.

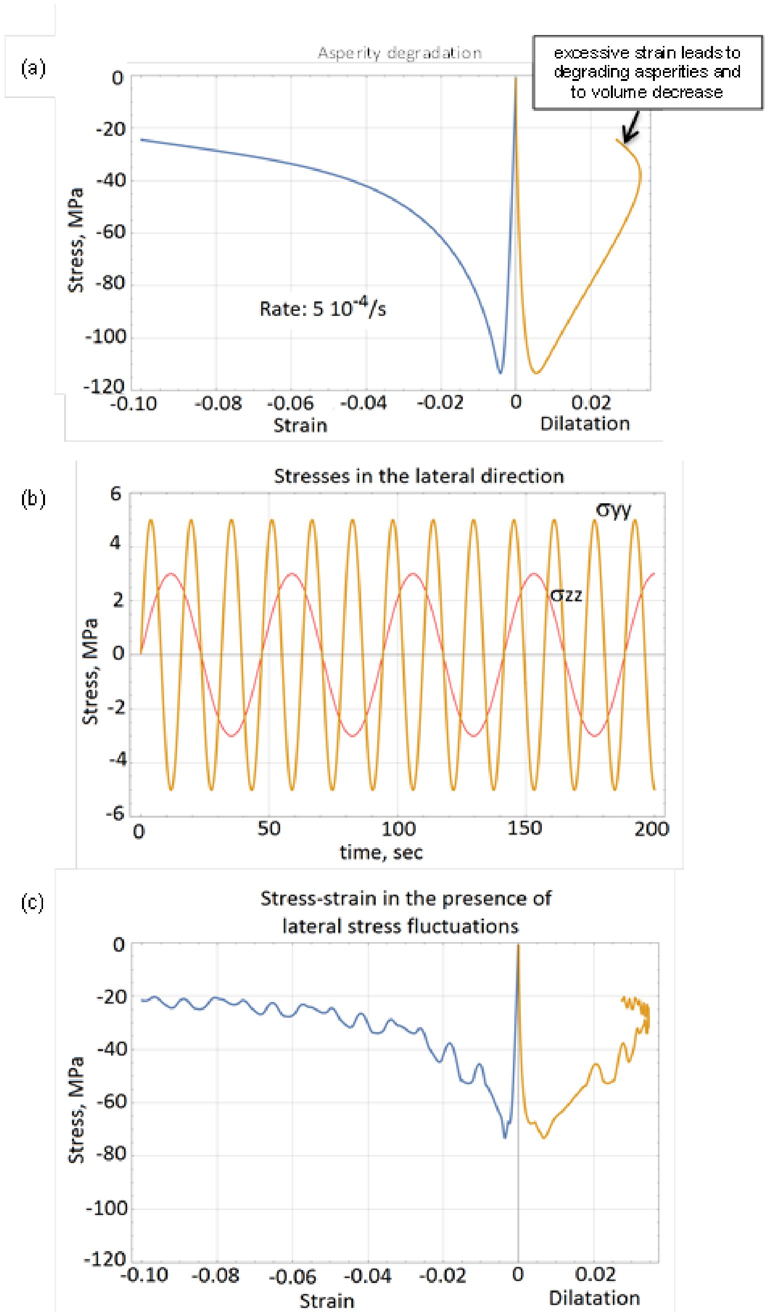

Figure 6. (a) Single element material response and dilatation in uniaxial compression with constant load. (b) Oscillating loads in lateral directions with different amplitudes and frequencies lead to (c) an oscillating, but robust material response.

3.2 Damage in Core Plug

Typically, rock samples from the subsurface (core plugs) are subjected to various laboratory tests. During uniaxial loading tests, material behavior is recorded, from which mechanical properties can be recovered. Loading is applied until the material fails. Depending on the geometry of the sample, it may experience fracture either due to shear bands or the boundary conditions may cause vertical cracking in addition to shear. We further validate the fracture model by applying it to a core plug sample in a large-scale 3D finite-element analysis. We use 52,592 hexagonal elements to mesh a cylindrical core plug with 1 in (2.54 cm) diameter and 3 in (7.62 cm) in length. We assume frictionless upper and lower cylinder surfaces (Figure 7), and initially undamaged material with uniform properties. As observed in the single element analysis, the average stress reaches a peak value and, then, material degradation brings it down while a localized shear band is formed. Figures 7b and 7c show the finite-element mesh and the damage distribution at the end of the numerical experiment. Our model results reproduce the experimentally observed fracture mechanism.

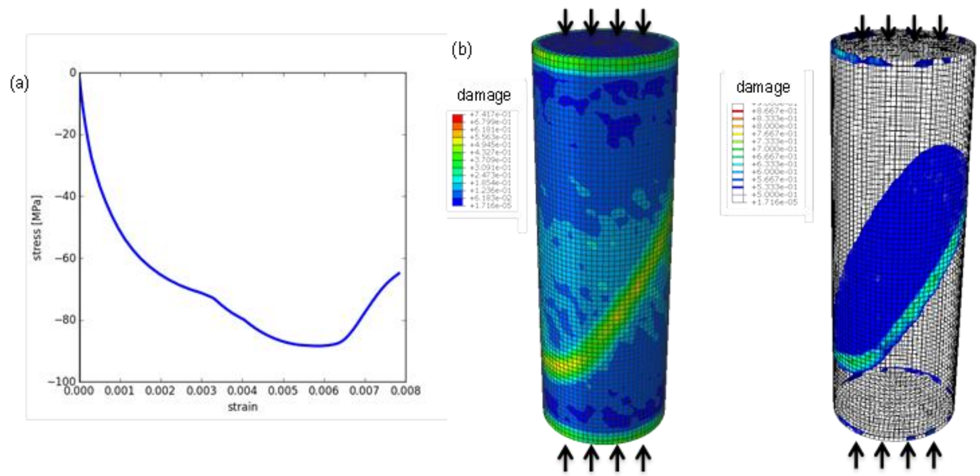

Figure 7. Core plug model without hydraulically-driven fractures. (a) Material response during uniaxial loading. (b) Localized damage band is visible on outer surface (left) and by means of isosurfaces (right).

3.3 Hydraulically-driven Fracture

Our objective is to predict the fracture processes caused by hydraulic pressurization of the borehole. First, we study the fracture processes under the conditions of plane strain analysis (Figure 8). We apply an unstructured finite-element mesh using hexahedral elements in a 10m x 10m x 1mm domain with significant mesh refinement near the wellbore. The fluid pressure in cracks is the wellbore pressure scaled down as a function of the distance from the wellbore. We introduce the far-field (large elements) and, in this manner, minimize the effects of external

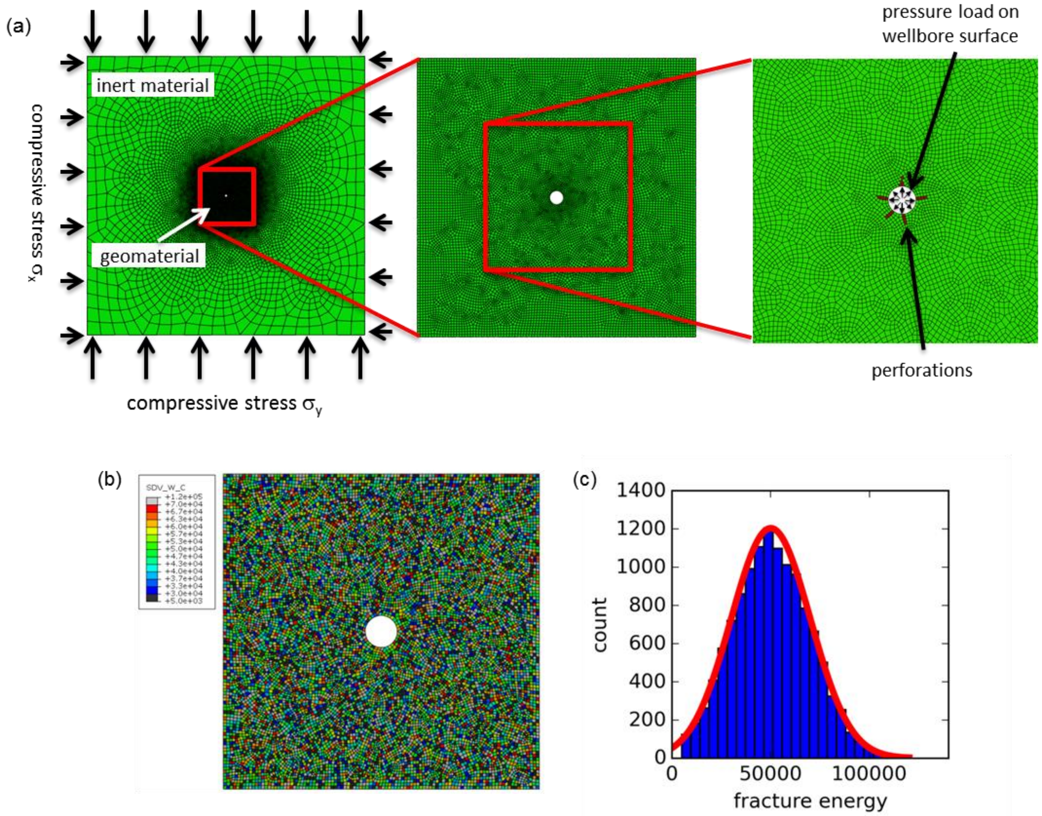

Figure 8. Model construction. (a) Mesh, material locations and boundary conditions/loads. Fracture energy (b) distribution and (c) histogram.

boundaries. Fracture energy is a stochastic property spatially distributed, as shown in Figures 8b and 8c. All other material properties are constant. The hydraulically pressurized material is prone to tensile cracking and shear induced damages. We consider three sets of tectonic stress, Figure 9. As shown, cracks propagate in the orientations defined by the minimum tectonic stress. We note that hydrostatic tectonic pressure does not lead to cracks with preferential orientations.

The processes of crack nucleation and propagation are associated with the conversion of internal energy to surface energy. Also, the rate of kinetic energy is an indicator for the existence of local dynamic instabilities. In Figure 10, we show contours of the kinetic energy rate. As shown, a burst of kinetic energy produces well-defined concentric waves. In this case, we do not include the far-field material, thus the boundary conditions reflect the waves back into the material.

Hydraulic stimulation is used to predict and, then, increase permeability in the reservoir. In our model, permeability is affected by interlinked branches of micro-cracks. We show results of three

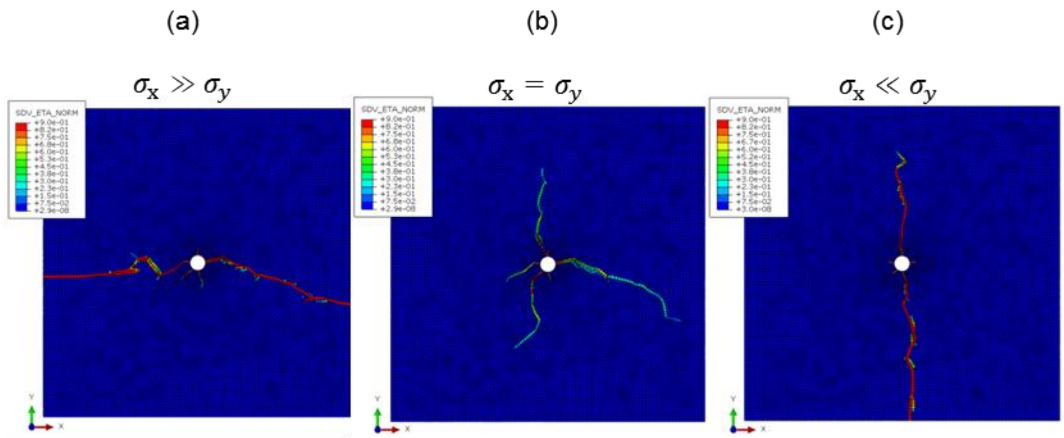

Figure 9. Damage patterns in the presence of different compressive far-field conditions. (a) $\sigma_x = 80$ MPa, $\sigma_y = 40$ MPa, (b) $\sigma_x = 40$ MPa, $\sigma_y = 40$ MPa, (c) $\sigma_x = 40$ MPa, $\sigma_y = 80$ MPa.

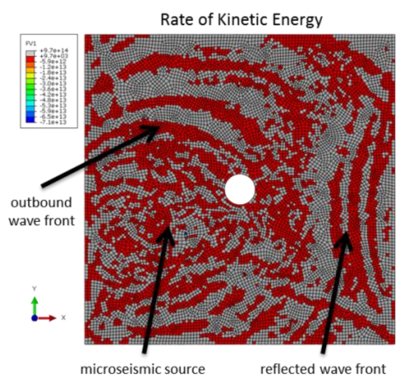

Figure 10. Distribution of rate of kinetic energy. For illustration purposes, this model is not embedded inside a large inert zone. This allows energy waves to be reflected at the model sides.

numerical simulations where we monitor the fracture-induced enhancement of permeability (Figure 11). In Figure 11a, permeability is increased due to friction-induced dilatation. Next, permeability is affected by tensile cracks (Figure 11b) and, lastly, we superimpose the two effects (Figure 11c). We notice that the friction-induced dilatation leads to a modest and, yet, relevant increase of permeability.

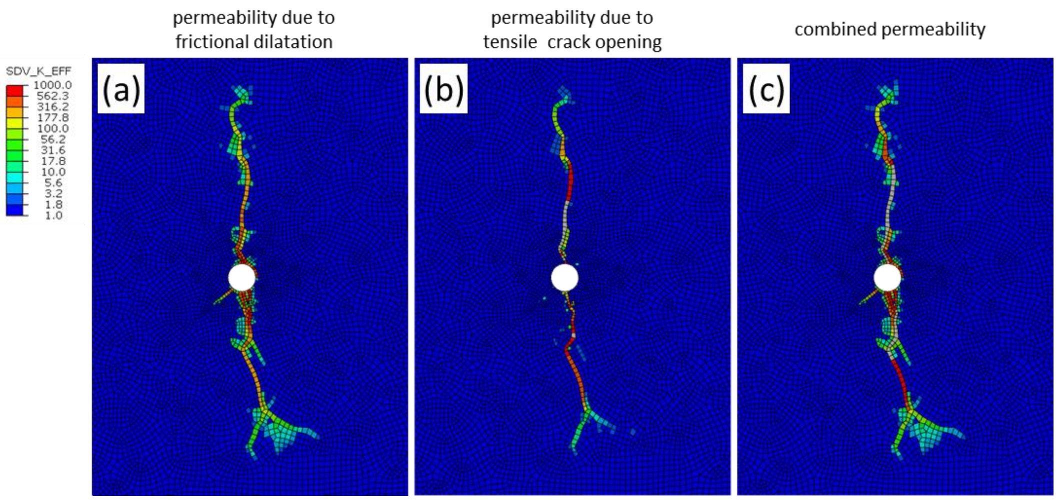

Figure 11. Distribution of permeability improvement caused by (a) frictional dilatation, (b) tensile crack opening, (c) both mechanisms.

In the next step, we construct a 3D model that is meshed using a fully unstructured mesh with 792,159 second-order tetrahedral elements (Figure 12). The spatial distribution of the fracture energy and the histogram are shown in Figures 12a and 12b. As in previous cases, the spatial distribution of fracture energy is drawn from the truncated normal distribution. This model contains a single perforation centered in the borehole line. Cross-sections of the perforations are shown in Figure 12c. Irrespective of the crack length, the crack tips are surrounded by diffuse damage. A more complex case is studied for a borehole that contains three equally spaced perforations along the borehole (Figure 13). As before, we show the distribution of fracture energy (Figures 13a and 13b). As pressure increases, fractures grow and at high pressure, the damage zones coalesce into a single fracture (Figure 13c).

4. Conclusions

We have developed a mechanisms-based fracture model for geological materials and implemented the model in Abaqus/Explicit as a material subroutine. First, we evaluate the material behavior for a single element under various loading conditions. In this manner, we demonstrate key characteristics of rock behavior and failure in compression, tension, and non-proportional loading. Also, we test the model for various strain rates. Using an assembly of elements in 3D, we predict the responses in a core plug. At this point, we have gained full confidence that the model is ready for the prediction of fracture mechanisms near the pressurized borehole. Complex two and three dimensional analyses show that our model correctly reproduces the observed behaviors and fracture of geological materials and properly estimates enhancements of permeability.

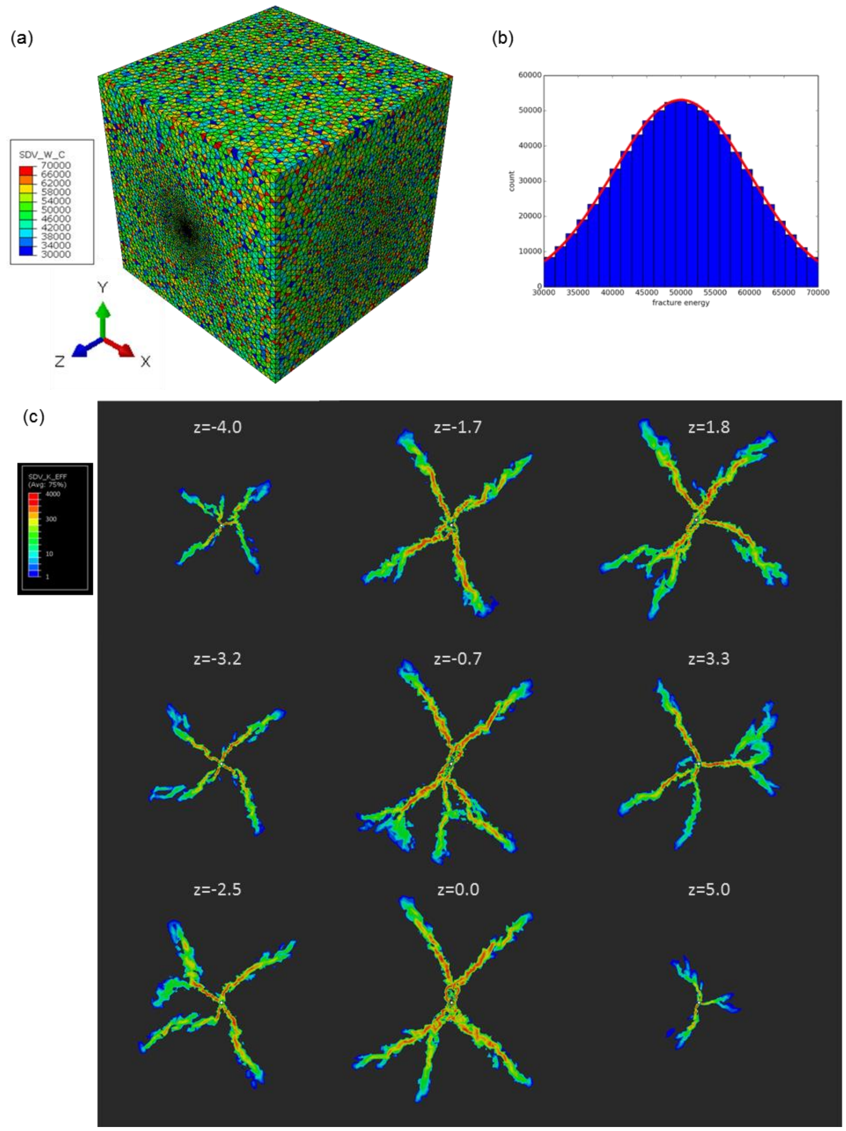

Figure 12. 3D model with tetrahedral mesh. Fracture energy (a) distribution and (b) histogram. (c) Permeability increase contoured on cross-sections at different z-coordinates, indicated with distance (in meters) to perforation location at model center

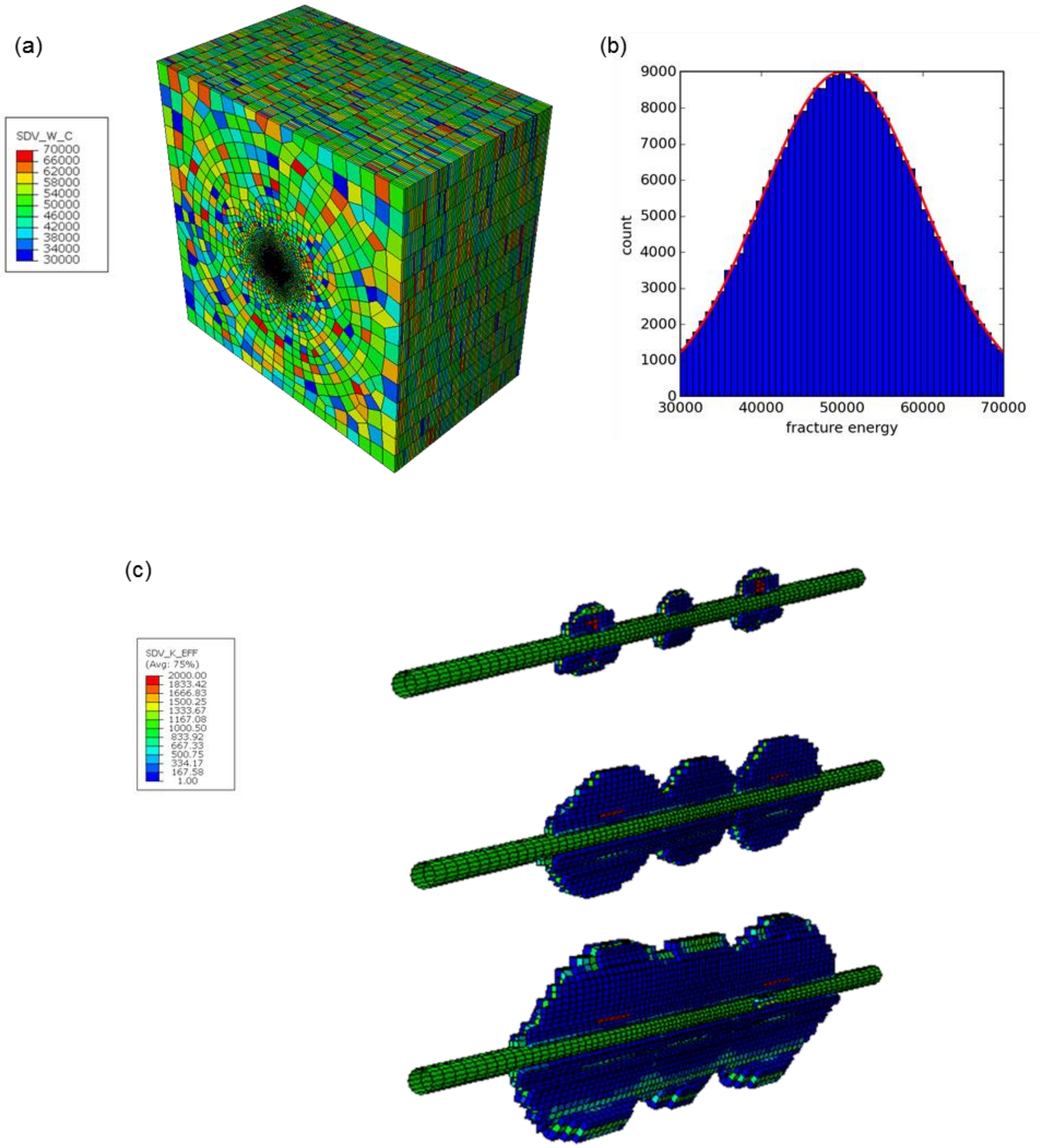

Figure 13. 3D model with hexahedral mesh. Fracture energy (a) distribution and (b) histogram. (c) Coalescence of three hydraulically driven fractures shown at different time steps.

5. Acknowledgements

The authors thank Baker Hughes management for the permission to publish the Modified Mohr-Coulomb Fracture model and Alek and Research Associates for the contribution in preparing this article. Also, the authors acknowledge Alek and Research Associates for the construction of the Modified Mohr-Coulomb Fracture model for Baker Hughes.

6. References

1. Dowding, C.H., Zubelewicz, A., O'Connor, K.M., and Belytschko, T.B., "Explicit Modeling of Dilation, Asperity Degradation and Cyclic Seating of Rock Joints", Computers and Geotechnics, 11, pp. 209- 227, 1991.
2. Ghanizadeh, A., Amann-Hildenbrand, A., Gasparik, M., Gensterblum, Y., Krooss B.M. and Littke, R., Experimental study of fluid transport processes in the matrix system of the European organic-rich shales: II. Posidonia Shale (Lower Toarcian, northern Germany), Int. J. Coal Geology, 123, 20-33, 2013.
3. Zubelewicz, A., O'Connor, K.M., Dowding, C.H., Belytschko, T.B., and Plesha, M., "A Constitutive Model for Cyclic Behavior of Dilatant Rock Joints", Proc. 2nd Int. Conference on Constitutive Laws for Engineering Materials: Theory and Applications, Tucson, Arizona, pp. 1137-1144, 1987.
4. Zubelewicz, A., "Overall Stress and Strain Rates for Crystalline and Frictional Materials", Int. Journal of Non-Linear Mechanics, 25, 389-393 (1990).
5. Zubelewicz, A. Micromechanical Study of Ductile Polycrystalline Materials. J. Mech. Phys. Solids 41, 1711-1722 (1993).
6. Zubelewicz, A., Thompson, D.G., Ostoja-Starzewski, M., Ionota, A., Shunk, D., Lewis, M.W., Lawson, J.C., Kale, S. and Koric, S. "Fracture model for cemented aggregates", AIP Advances, 3, 012119 (2013).
7. Zubelewicz, A., Rougier, E., Ostoja-Starzewski, M., Knight, E.E., Bradley, C. and Viswanathan, H.S., "Dynamic behavior and fracture of materials", Int. J. Rock Mech. and Mining Sci., 72, 277-282 (2014).